# Multi-Scale Displacement Field Measurements of Compressed Mineral Wool Samples by Digital Image Correlation

François Hild, Bumedijen Raka, Maud Baudequin, Stéphane Roux, Florence Cantelaube

▶ To cite this version:

François Hild, Bumedijen Raka, Maud Baudequin, Stéphane Roux, Florence Cantelaube. Multi-Scale Displacement Field Measurements of Compressed Mineral Wool Samples by Digital Image Correlation. Applied optics, 2002, IP 41, pp.6815-6828. 10.1364/AO.41.006815 . hal-00002901

HAL Id: hal-00002901
https://hal.science/hal-00002901v1

Submitted on 20 Sep 2004

# Multi-Scale Displacement Field Measurements of Compressed Mineral Wool Samples by Digital Image Correlation

François Hild, Bumedijen Raka

LMT-Cachan
ENS de Cachan/CNRS-UMR 8535/Université Paris 6
61 avenue du Président Wilson, F-94235 Cachan Cedex,
France

*Francois.Hild,Bumedijen.Raka@lmt.ens-cachan.fr*

Maud Baudequin, Stéphane Roux

Laboratoire Surface du Verre et Interfaces
UMR CNRS/Saint-Gobain
39 quai L. Lefranc, F-93303 Aubervilliers Cedex, France

Florence Cantelaube

CRIR, 19 rue Emile Zola, F-60290 Rantigny, France

*Maud.Baudequin,Stephane.Roux@saint-gobain.com,*
*Florence.Cantelaube@saint-gobain.com*

We propose a multi-scale approach to determine the displacement field by digital image correlation. The displacement field is first estimated on a coarse resolution image and progressively finer details are introduced in the analysis as the displacement is more and more securely and accurately determined. Such a scheme has been developed to increase the robustness, accuracy and reliability of the image matching algorithm. The procedure is used on two different types of examples. The first one deals with a representative image that is deformed exactly to assess the intrinsic performances. In particular, the maximum measurable strain is determined. The second case deals with a series of pictures taken during compression experiments on mineral wool samples. The different steps of the procedure are analyzed and their respective role is assessed. Both reflection and transmission images are tested.

**OCIS codes:** 070.2590, 100.2000, 100.5010, 120.3940, 120.6150, 040.1520.

## 1. Introduction

In recent years, the development of efficient tools for field velocimetry, aiming at fluid flow visualization [1], has been quite important. Digital Particle Image Velocimetry (DPIV) [2, 3, 4, 5], Digital Image Correlation (DIC) [6, 7] or more generally Correlation Imaging Velocimetry (CIV) [8, 9] have proven to be an efficient and robust tool whose precision can be extended much below the pixel accuracy. The spirit of the method is to look for the maximum correlation between small zones extracted from the ‘deformed’ and reference images. The translation, which corresponds to the maximum correlation, can be obtained for different positions of the zone of interest. This allows for the determination of a displacement field which is piecewise constant. The correlations are evaluated either in the reference space [6, 10] or Fourier space [2, 3, 11, 12, 13] and the extensive use of Fast Fourier Transforms (FFT) is very effective in reducing the computation cost.

Some applications concern soft solids where strain gauges can be difficult to position or may disturb the response of the material because of stiffness variations (e.g., mineral wool [9], paper and wood [14], polymers [15, 16]). In most experiments in solid mechanics, the random texture used to determine the displacement field is not changing during the test, e.g., cracks may appear, but the alterations are localized and hardly induce any artifacts. It can be noted that the texture is either natural (e.g., many materials at high magnification) or artificial (e.g., by spraying paint). In some applications however, this is no longer the case, e.g., during a compression test of mineral wool samples where pictures are obtained in transmission. As the sample is compressed, the average texture intensity decreases when the aperture is not altered. In addition, the change in intensity due to the compression alters the absorption and scattering of light in the material, and hence increases the distortion between the images in a complex and heterogeneous manner. As a consequence, classical methods fail to measure accurately the strain fluctuations in such situations.

One purpose of the present study is to propose a multi-scale approach to increase the maximum detectable displacement compared to conventional DIC techniques. Since texture variations are suspected to occur, a special procedure is developed to deal with this effect, which can be probed in particular, for the above-mentioned mineral wool samples. Section 2 introduces two basic tools needed to develop a DIC technique, namely, displacements measured by a correlation algorithm and the choice of a strain descriptor in the finite deformation framework. In Section 3, the basic DIC algorithm is recalled. A sub-pixel procedure is used to increase the sensitivity for accurate strain measurements. The maximum detectable displacement is evaluated on a deformed picture, which is artificially generated. A multi-scale approach is then developed to increase the maximum detectable displacement, without affecting the minimum measurable strain. Section 4 deals with artificially deformed images to analyze the effect of different steps introduced in the multi-scale correlation algorithm. Section 5 is devoted to the analysis of two sets of compression experiments performed on mineral wool samples, respectively. This material allows for large strains, and various exposure modes. Moreover, being heterogeneous, it displays fluctuations in local strains. It thus constitutes a difficult test case for the analysis. Mineral wool is a material for which better mechanical performances can be reached by mastering the microstructure and homogeneity. In particular, for medium to high density products, the wool is “crimped” to get better mechanical performance. Crimping is a uniaxial compression along the line direction performed on the wool by forcing it through progressively slower advancing compression belts. This industrial process, suited to continuous production, induces buckling of the denser planes and hence changes the orientation of initially horizontal fibers to vertical or at least more isotropic distributions. Hence, it is of interest to be able to resolve the local strain, or irreversible part of the strain, in order to relate it to the local ‘microstructure’ such as material density or fiber orientation. This is especially important for crimped products and where quality factors for the texture can be derived from the local analysis of the irreversible strain, and its relationship to morphological features.

## 2. Preliminaries

### A. Displacement measurement by image correlation

To determine the displacement field of one image with respect to a reference image, one considers a sub-image (e.g., a square region) which will be referred to as a Zone Of Interest (ZOI) or interrogation window. The aim of correlation method is to match the ZOI in the two images (Fig. 1). The reference image corresponds to the texture of a stone wool sample. The displacement of one ZOI wrt. the other one is a two-dimensional shift of an intensity signal digitized by a CCD camera. To estimate a shift between two signals, one of the standard approaches is based on a correlation function. One considers signals $g(\boldsymbol{x})$ which are merely perturbations of a shifted copy $f(\boldsymbol{x} - \boldsymbol{u})$ of some reference signal $f(\boldsymbol{x})$

$$g(\boldsymbol{x}) = f(\boldsymbol{x} - \boldsymbol{u}) + b(\boldsymbol{x}) \tag{1}$$

where $\boldsymbol{u}$ is an unknown in-plane displacement vector assumed to be constant locally (i.e., independent of the position $\boldsymbol{x}$) and $b(\boldsymbol{x})$ a random noise (e.g., photon noise, readout noise, dark current noise for CCD cameras [17]). To evaluate the displacement $\boldsymbol{u}$, one may minimize the norm of the difference between $f(\boldsymbol{x} - \boldsymbol{v})$ and $g(\boldsymbol{x})$ with respect to a trial displacement $\boldsymbol{v}$

$$\min_{\boldsymbol{v}} ||g - f(. - \boldsymbol{v})||^2 \tag{2}$$

where '.' denotes a dummy variable. The functional $||g - f(. - \boldsymbol{v})||^2$ can be used in other instances when the displacement field, instead of being constant, is either affine or developed in terms of a truncated Fourier series [9]. These variational formulations are mainly based on the optical flow equation. A spatial regularization was introduced by Horn and Schunck [19] and consists in a looking for *smooth* displacement solutions. However, this method is not appropriate for problems dealing with discontinuities in the apparent displacement [20]. In the latter case, the quadratic penalization is replaced by 'smoother' penalizations based on robust statistics [21, 22, 23]. Furthermore, when dealing with deformable solids, other regularization techniques are to be introduced such as the one based on the strain energy [24].

In fact, any class of displacements may be introduced and a Taylor expansion yields a linear system in the unknown displacement components [18]. If one chooses the usual quadratic norm $||f||^2 = \int\int_{-\infty}^{+\infty} |f(\boldsymbol{x})|^2 \ \mathrm{d}\boldsymbol{x}$, it corresponds to the so-called MQD method used in experimental fluid mechanics [25] when implemented directly with a constant trial displacement. With this norm, the previous minimization problem is *equivalent* to maximizing the quantity $h(\boldsymbol{v})$

$$h(\boldsymbol{v}) = (g \star f)(\boldsymbol{v}) \equiv \int_{-\infty}^{+\infty} \int_{-\infty}^{+\infty} g(\boldsymbol{x}) f(\boldsymbol{x} - \boldsymbol{v}) \mathrm{d}\boldsymbol{x} \tag{3}$$

where $\star$ denotes the cross-correlation operator. Furthermore, when $b$ is a white noise, the previous estimate is optimal. The displacement maximizing the cross-correlation product will be denoted by $\boldsymbol{w}$ and corresponds to an evaluation of the unknown displacement vector $\boldsymbol{u}$. The computation of a cross-correlation product can be performed either in the original space or in Fourier space, by using an FFT

$$g \star f = \mathrm{FFT}^{-1} \left( \mathrm{FFT}[g] \, \overline{\mathrm{FFT}[f]} \right) \tag{4}$$

where the complex conjugate is overlined. In the following sections, extensive use of the cross-correlation product will be made. It will always be evaluated via Fourier transforms to speed-up the computations. Numerous works have addressed the issue of the periodicity of the image implicitly assumed when using FFT. In particular, there lies the main difference between the Maximum Quadratic Difference (MQD) method and standard correlation based evaluations, as discussed in details in Ref. [25]. In the present work, we deal with this problem through windowing filters (e.g., Hanning window or edge-blurring) as discussed further down.

### B. Strain measures

Finite strain measures are needed since the strain level will be greater than a few percents. These measures are built by using the deformation gradient tensor $\boldsymbol{F}$ relating an infinitesimal vector $\mathrm{d}\boldsymbol{x}_0$ in the reference configuration ($\Omega_0$) to $\mathrm{d}\boldsymbol{x}$ in the deformed configuration ($\Omega$)

$$\mathrm{d}\boldsymbol{x} = \boldsymbol{F}\,\mathrm{d}\boldsymbol{x}_0 \tag{5}$$

so that the tensor $\boldsymbol{F}$ can be related to the displacement gradient $\boldsymbol{\nabla u}$ by

$$\boldsymbol{F} = \mathbf{1} + \boldsymbol{\nabla u}, \tag{6}$$

where $\mathbf{1}$ is the second order unit tensor. For Lagrangian measures, they can be expressed by using the strain tensors $\boldsymbol{E}_m$ [26]

$$\boldsymbol{E}_m = \begin{cases} \frac{1}{2m}\left(\boldsymbol{C}^m - \mathbf{1}\right) & \text{when} \quad m \neq 0 \\ \\ \frac{1}{2}\ln\left(\boldsymbol{C}\right) & \text{when} \quad m \to 0^+ \end{cases} \tag{7}$$

where $\boldsymbol{C} = \boldsymbol{F}^t\,\boldsymbol{F}$ denotes the right Cauchy-Green deformation tensor, and $^t$ the transposition operator. When $m = 1$, the Green-Lagrange strain tensor is obtained, $m = 1/2$ is the Cauchy-Biot (or nominal) strain tensor and yields $\Delta L/L_0$ for a uniaxial elongation, where $L_0$ is a reference (or gauge) length and $\Delta L$ the length variation. The case $m \to 0^+$ corresponds to the logarithmic (or Hencky) strain tensor. The latter is the only *additive* strain measure. By definition, all these strains are equal to zero for a rigid translation (i.e., $\boldsymbol{F} = \mathbf{1}$ and $\boldsymbol{C} = \mathbf{1}$) or a rigid rotation (i.e., $\boldsymbol{F} = \boldsymbol{R}$ and $\boldsymbol{C} = \mathbf{1}$), where $\boldsymbol{R}$ is an orthogonal tensor. When the amplitude of the body motion is small as well as the strain gradient, all measures converge towards the so-called infinitesimal strain tensor $\boldsymbol{\varepsilon}$ defined as

$$\boldsymbol{\varepsilon} = \frac{1}{2}\left[\boldsymbol{\nabla u} + (\boldsymbol{\nabla u})^t\right]. \tag{8}$$

In the following, for the sake of simplicity, the nominal strain tensor will be used and will be denoted by $\boldsymbol{E} = \boldsymbol{E}_{1/2}$.

## 3. A multi-scale approach in digital image correlation

### A. Conventional approach

In practice, two images are considered. The first one, referred to as 'reference image' and the second one, called 'deformed image'. The following algorithm is summarized in the flow chart of Fig. 2. To determine the average displacement, one extracts the largest value $P$ of an inscribed region of interest (ROI) of size $2^P \times 2^P$ centered in the reference image. The same ROI is considered in the deformed image. A first FFT correlation is performed to determine the average displacement $\boldsymbol{w}_0$ of the deformed image with respect to the reference image. This displacement vector is expressed by an integer number of pixels and is obtained as the maximum of the cross-correlation function evaluated for each pixel of the ROI. This first prediction enables one to determine the maximum number of pixels that belong to both images. The ROI in the deformed image is now centered at a point corresponding to displaced center of the ROI in the reference image by an amount $\boldsymbol{w}_0$.

The user usually chooses the size of the ZOIs by setting the value of $p < P$ so that its size is $2^p \times 2^p$ pixels. To map the whole image, the second parameter to choose is the shift $\delta = ||\boldsymbol{\delta x}|| = ||\boldsymbol{\delta y}||$ between two consecutive ZOIs: $1 \leq \delta \leq 2^p$ pixels. This parameter defines the mesh formed by the centers of each ZOI used to analyze the displacement field (Fig. 1). The analysis is then performed for each ZOI *independently*. A first FFT correlation is carried out and a first value of the in-plane displacement correction $\Delta \boldsymbol{w}$ is obtained. The components of $\Delta \boldsymbol{w}$ are again integer numbers so that the ZOI in the deformed image can be displaced by an additional amount $\Delta \boldsymbol{w}$. The displacement residues are now less than 1/2 pixel in each direction. A sub-pixel iterative scheme can be used.

This first procedure is well-adapted for small strain levels. If no additional positioning is performed, to be successful, the norm of the displacement correction $\Delta \boldsymbol{w}$ has to be limited. Otherwise, the correlation fails since there is not enough information to determine the correction. To illustrate this effect, a conventional analysis is performed between the reference image ($512 \times 512$ pixels, 8-bit digitization) shown in Fig. 1 and an artificially deformed image. The reference image corresponds to a stone wool sample to be artificially deformed along the vertical direction (i.e., $\boldsymbol{j}$). The deformed image is computed by using Eq. (1), and a linear interpolation of the gray levels to evaluate the pixel value in the deformed image. No noise is added (i.e., $b(.) = 0$) but the signal is digitized by using the same 8-bit coding. The same $512 \times 512$ pixel ROI is considered and different values for $p$ are investigated. In the present case, the initial correction $\boldsymbol{w}_0$ is found to be vanishingly small. Consequently, the middle height of the image is a line of symmetry for the displacement field. Figure 3 shows the standard deviation of the vertical displacement $w_y$ for each vertical position $y$ of the ZOIs when $\delta = 16$ pixels. The smaller the standard deviation, the more accurate the displacement evaluation. For symmetry reasons, the standard deviation $\overline{\overline{w}}_y$ is interpolated by a parabolic polynomial defined by

$$\overline{\overline{w}}_y(y) = \alpha(p) + \beta(p)(255.5 - y)^2 \tag{9}$$

where $\alpha$ and $\beta$ are constants dependent upon the size of the ZOIs (i.e., $2^p \times 2^p$ pixels). An arbitrary limit $\overline{\overline{w}}_{\max}$ is defined such that below the latter, the evaluation is considered to be accurate and above which it is questionable. A value of 1 pixel is chosen. Consequently, displacement corrections $\Delta w$ varying within the range ±7 pixels can be measured accurately when $p = 4$ and ±13 pixels when $p = 5$. For higher values of $p$, no intersection is found when the average strain is equal to 0.05 (Fig. 3). As a first approximation, a displacement correction greater than $\pm 3 \times 2^{p-3}$ pixels leads to a loss of accuracy in its evaluation. It can be noted that when a value of 0.6 pixel is chosen, the displacement estimate is more accurate than in the previous case and the 'quarter rule' is obtained (i.e., the maximum measurable displacement is equal to one quarter of the size of the ZOI [27]). These results shows that the first pixel evaluation $\boldsymbol{w}_0$ is crucial in allowing to increase the admissible range of measurable displacements. Table 1 shows that the higher $p$, the more accurate the strain evaluation. However, the gain between $p = 6$ and $p = 7$ is minimal. If one increases $p$ too much, then one averages over a larger surface the displacement. The measurement of fluctuations with respect to an average field is limited (e.g., in tension/compression tests). Consequently, a good compromise in this example is given by $p = 6$. Lastly, for images such that the maximum distance of horizontal or vertical centers of ZOIs is of the order of 1024, a maximum measurable strain is equal to $3 \times 2^{p-12}$, which is of the order of 0.05 when $p = 6$.

It can be noted that small strain levels can be accurately measured by using a sub-pixel algorithm. An additional cross-correlation is performed. A sub-pixel correction of the displacement $\delta\boldsymbol{w}$ is obtained by determining the maximum of a parabolic interpolation of the correlation function. The interpolation is performed by considering the maximum pixel and its eight nearest neighbors. Therefore, one obtains a sub-pixel value. By using the 'shift-modulation' property of Fourier transform, which is nothing but a phase change, the deformed ZOI can be moved by an amount $-\delta\boldsymbol{w}$. Since an interpolation is used, one may induce some (small) errors requiring to re-iterate by considering the new 'deformed' ZOI until convergence. The procedure used checks whether the maximum of the interpolated correlation function increases as the number of iterations increases. Otherwise, the iteration scheme is stopped.

In order to limit the influence of edge effects, a windowing of the ZOI can be performed [16]

$$\widetilde{ZOI} = ZOI\ \chi \otimes \chi \tag{10}$$

where $\widetilde{ZOI}$ denotes the windowed $ZOI$, $\otimes$ the dyadic product and $\chi$ the one-dimensional modified Hanning window

$$\chi(I) = \begin{cases} \dfrac{1}{2}\left[1 - \cos\left(\dfrac{4\pi I}{2^p - 1}\right)\right] & \text{when} \quad 0 \leq I < 2^{p-2}, \\ 1 & \text{when} \quad 2^{p-2} \leq I < 3 \times 2^{p-2}, \\ \dfrac{1}{2}\left[1 - \cos\left(\dfrac{4\pi I}{2^p - 1}\right)\right] & \text{when} \quad 3 \times 2^{p-2} \leq I < 2^p - 1. \end{cases} \tag{11}$$

The value $2^{p-2}$ is optimal to minimize the error due to edge effects and to have a sufficiently large number of data unaltered by the window. In the following, a second window is introduced. It consists in constructing a periodic ZOI, $\widehat{ZOI}$, by averaging the pixels on the edges of the initial ZOI (i.e., 'blurring' the edges)

$$\widehat{ZOI} = W\, ZOI\, W \tag{12}$$

where the matrix $W$ is equal the identity matrix apart from the four 'corners', which are equal to 1/2. The effect of the two windows on the accuracy of the strain measurement will be tested later on. The procedure, CORRELI$^{LMT}$, is implemented in MATLAB™ [28]. The sub-pixel procedure allows for strain levels less than $10^{-4}$ to be measured accurately with an 8-bit camera [16, 29]. For many materials (e.g., metals and alloys, composites), a strain range varying between $10^{-4}$ and $5 \times 10^{-2}$ is sufficient to analyze tension/compression tests. However mineral wool or polymers can experience strain levels greater than the previous levels. The aim of the following developments is to increase the maximum detectable displacement without altering the intrinsic sensitivity of the sub-pixel correlation procedure. To achieve this goal, a multi-scale approach is now developed.

### B. Definition of image and displacement scales

To increase the maximum measurable displacement between two pictures, two major steps are added. Contrary to adaptative local window shifting techniques [30, 31], in the present approach, different scales are introduced: the finer scale is that of the original picture (i.e., typically 0.5 to 1 Mpixels with classical CCD cameras). It will be referred to as scale no. 0 (Fig. 4). In this image, the ROI is a smaller part of it: it defines the region over which the multi-scale procedure will be applied. This corresponds to scale no. 1 (Fig. 4). Let $\boldsymbol{d}_{01}$ denote the vector joining the origin of the ROI to that of the image frame. If no rigid body rotations are assumed, the displacement field $\boldsymbol{u}(\boldsymbol{x}_0)$ in a homogeneous deformation test is expressed as

$$\boldsymbol{u}(\boldsymbol{x}_0) = \boldsymbol{A}\,\boldsymbol{x}_0 + \boldsymbol{a} \tag{13}$$

with

$$\boldsymbol{A} = \begin{bmatrix} A_{xx} & 0 \\ 0 & A_{yy} \end{bmatrix} \tag{14}$$

where $\boldsymbol{A}$ is an in-plane tensor that characterizes the average deformation (in the present case, $\boldsymbol{F} = \boldsymbol{A}$), and $\boldsymbol{a}$ a constant displacement vector. The right Cauchy-Green deformation tensor can be written as

$$\boldsymbol{C} = \boldsymbol{A}^2 \,, \tag{15}$$

and hence, in this particular case, the tensor $\boldsymbol{A}$ is nothing but the nominal strain tensor, $\boldsymbol{E} = \boldsymbol{A}$.

In the frame of the ROI where a current point is located by the vector $\boldsymbol{x}_1 = \boldsymbol{x}_0 - \boldsymbol{d}_{01}$, the previous displacement is written as

$$\boldsymbol{u}(\boldsymbol{x}_1) = \boldsymbol{A}\,\boldsymbol{x}_1 + (\boldsymbol{a} + \boldsymbol{A}\,\boldsymbol{d}_{01}) \,. \tag{16}$$

One determines the largest values $P$ and $Q$ of the sub-ROI of size $2^P \times 2^Q$ centered and inscribed in the ROI. This sub-ROI is adapted to FFT algorithms and defines scale no. 2 (Fig. 4). Let $\boldsymbol{d}_{12}$ denote the vector joining the origin of the sub-ROI to that of the ROI. In the frame of the sub-ROI ($\boldsymbol{x}_2 = \boldsymbol{x}_1 - \boldsymbol{d}_{12}$), one has

$$\boldsymbol{u}(\boldsymbol{x}_2) = \boldsymbol{A}\,\boldsymbol{x}_2 + [\boldsymbol{a} + \boldsymbol{A}\;(\boldsymbol{d}_{01} + \boldsymbol{d}_{12})] \,. \tag{17}$$

From scale no. 3 on, each scale transition is characterized by the definition of super-pixels (Fig. 4). The super-pixels are defined recursively from one scale to the next by averaging the gray levels of 2 × 2 neighboring pixels. Alternatively, one could use the Fourier transform images to filter them. Both procedures should give comparable results, and in the following the real-space coarse-graining super-pixels are used. On scale no. $n \geq 3$, the displacement field is now expressed as

$$\boldsymbol{u}(\boldsymbol{x}_n) = \boldsymbol{A}\,\boldsymbol{x}_n + 2^{2-n}\left[\boldsymbol{a} + \boldsymbol{A}\,\left(\boldsymbol{d}_{01} + \boldsymbol{d}_{12}\right)\right]. \tag{18}$$

Equations (13), (16), (17) and (18) show that any scale transition leaves the magnitude of strain *unchanged* whereas the average displacement decreases starting from scale no. 3. In Fig. 4, the different notations used are summarized. A reference sub-ROI is shown and two super-images on coarser scales. This procedure is carried out until the minimum size of the sub-image is equal to 128 pixels. The size of the ZOI is such that $p = 5$ on scales no. 2 to $n$. On scale no. 1, the user chooses the size of the ZOIs. An iterative correlation algorithm is now applied on each scale. The aim is to first evaluate interpolated displacements (i.e., $\boldsymbol{A}$ and $\boldsymbol{a}$) on the higher scales down to scale no. 1 for which the displacement amplitude may be greater than the size of the ZOI on scale no. 1.

The maximum detectable displacement amplitude is denoted by $\Delta w_{\max} \approx 3 \times 2^{p-2}$ pixels (see Section 3.A). This value is *independent* of the scale considered. It is an intrinsic property of the correlation procedure. It follows that the maximum measurable strain $E_1 = \max(A_{xx}, A_{yy})$ on scale no. 1, when no multi-scale procedure is used, is expressed as

$$E_1 = \frac{\Delta w_{\max}}{(N-1)\delta} \tag{19}$$

where $N$ is the maximum number of horizontal or vertical centers of ZOIs. If $(N-1)\delta \approx 512$ pixels, then four scales can be defined so that the size of the ROI on scale no. 4 is: $L_4 = 128$ pixels. Consequently, the maximum detectable strain $E_4$ on scale no. 4 is

$$E_4 = \frac{\Delta w_{\max}}{L_4}, \tag{20}$$

which can be of the order of four times the value on scale no. 1. Since the strain tensor $\boldsymbol{A}$ remains unaltered by *any* of the considered scale transitions, this result shows the benefit of using a multi-scale approach. The strain resolution is unaltered when a sub-pixel procedure is used and the maximum value doubles for each scale transition $n \geq 3$. Furthermore, an iterative scheme will improve the assessment for large displacements as discussed in the next section.

### C. Multi-scale correlation algorithm

The multi-scale correlation algorithm is summarized in the flow chart of Fig. 5. Starting on the highest (i.e., coarser) scale, for which the sub-image size is at least equal to 128 super-pixels, a first correlation is performed. From this first computation, the displacement field is interpolated according to Eq. (18) as

$$\boldsymbol{u}_n(\boldsymbol{x}_n) = \boldsymbol{B}_n\, \boldsymbol{x}_n + \boldsymbol{b}_n \tag{21}$$

where $\boldsymbol{B}_n$ and $\boldsymbol{b}_n$ are first estimates of the strain tensor (of the form given in Eq. (14)) and rigid body displacement on scale no. $n$, respectively. To check this first estimate, the center of each ROI of the 'deformed' image is relocated according to these first estimates. A new correlation is performed and corrections to the previous displacement field are evaluated. The iterations are stopped as soon as there is no new correction between two iterations for *any* ZOI analyzed. This iterative procedure was implemented to make the displacement evaluation more robust. This robustness is a key to the success of the procedure. If ever the displacement is not properly evaluated on higher scales, there is no chance of getting a good final result: see Section 4. Consequently, the first evaluations have to be performed very carefully.

When the iterative procedure stops on scale no. $n$, it proceeds to scale no. $(n-1)$. Having identified a first estimate of the displacement field, it is used to position the ZOIs on scale no. $(n-1)$, according to the transformation rules inverted from those developed in the previous section. The same iterative scheme is followed for scales no. $(n-1)$ to 2. In practice, the user can choose between a first evaluation that is very fast since it remains on the pixel (or super-pixel) level, and an accurate evaluation requiring several iterations. On scale no. 1, the user selects either a pixel or a sub-pixel sensitivity of the displacement by following the above described sub-pixel procedure, thereby allowing for the measurement of small levels of strains as well as large levels that will be evaluated in the following sections.

When a sequence of more than two images is analyzed, two routes can be followed. The first one consists in considering the same reference image. It follows that the errors are not cumulated but there exists a maximum strain level above which the method fails (see Section 4). The second one considers that the reference image is the deformed image of the previous step (i.e., updating procedure). Under these hypotheses, there is no real limitation, apart from the fact that the errors are now cumulated. Strains of the order of 1 and more are routinely observed in a full-field assessment even with a conventional DIC technique [16].

### D. Control of the displacement estimate

The previous procedure has to be further improved to account for severe texture variations (see Section 5.B). In practice, small variations always occur but they are usually limited in magnitude. However, a compressive test dealing with mineral wool samples requires to treat explicitly this effect. Two different tests are therefore added.

First, it can be noted that, if the gray level is constant over a given ZOI, then a displacement estimation based on a correlation technique is impossible (the signal derivative is the key to minimizing the functional (2)). Consequently, the standard deviation of any ZOI has to be greater than one gray level. It can be noted that on the images of Fig. 6, this condition is not satisfied in the lower part. When the standard deviation is less than the chosen limit, the interpolated displacement obtained by the multi-scale procedure is used instead of any other estimate. This is true on any scale considered.

Second, to check that the correlation procedure was successful, an error indicator, which is *independent* of the correlation product or its normalized counterpart, is introduced. The following indicator

$$\eta = \left| \frac{\mathrm{MEAN}(ZOI_{\mathrm{ref}})}{\mathrm{MEAN}(ROI_{\mathrm{ref}})} - \frac{\mathrm{MEAN}(ZOI_{\mathrm{def}})}{\mathrm{MEAN}(ROI_{\mathrm{def}})} \right| \sqrt{\mathrm{MEAN}(ZOI_{\mathrm{ref}})\mathrm{MEAN}(ZOI_{\mathrm{def}})} \qquad (22)$$

turned out to be satisfactory, where the subscript $_{\mathrm{ref}}$ refers to the reference image and $_{\mathrm{def}}$ to the deformed image when convergence was obtained. Hence, a second test associated with $\eta$ is added: when $\eta \geq 4$ gray levels for 8-bit pictures, the correlation is considered as unsuccessful and the correlated displacement is again preferred. This indicator allows for the correction due to the average intensity change during a test and is expressed in terms of gray levels thanks to the square root part.

## 4. Test on artificially deformed images

In this section, the reference image of Fig. 1 is used to evaluate the intrinsic performances of the algorithm. The images are again deformed artificially with the same procedure as that used to obtain the results of Fig. 3. Figure 4 shows the sub-ROI of the reference image and the corresponding super-images for scales nos. $n = 3, 4$. When a strain of 0.05 is applied and a sub-pixel evaluation is chosen with no iteration, the effect of windowing can be discussed.

When no window is used, an average strain of 0.0493±0.0001[1] is obtained. When the modified Hanning window (Eq. (11)) is implemented, an average strain of 0.0494 ± 0.0001 is measured. Finally, when the edge-blurring procedure (Eq. (12)) is preferred, the average strain is equal to $0.0496 \pm 7 \times 10^{-5}$. The last measurement is the most accurate. The other ones are also acceptable thanks to the multi-scale procedure.

Figure 7 shows the results obtained by the multi-scale procedure for a nominal strain of 0.35 when $p = 4$ and $\delta = 16$ pixels. The predicted value is 0.3501 ± 0.0001 when the sub-pixel option is used and 0.3496 ± 0.0001 when the pixel option is used. For the sub-pixel option, the standard deviation ranges between 0.13 and 0.26 pixel (average value: 0.2 pixel) and is less than the prescribed limit. It follows that all the measurements are considered to be accurate. This case is completely out of reach for a conventional DIC technique (see Section 3.A). Because the prescribed and interpolated displacement fields are both bi-linear, the present approach allows for displacement amplitudes greater than the size of the ZOI. In the example, the displacement amplitude (i.e., 120 pixels) is 7.5 times greater than the ZOI size (i.e., 16 pixels). The limitation is now given by the highest scale (i.e., $n$) as opposed to scale no. 1 in the conventional DIC technique (in the present case, $n = 4$). Figure 8 shows how the average strains evolve during the iterations on each scale. It can be seen that even though the first estimate is only about one half of the actual solution, it is sufficient to get a good result at the end of the computation. In this particular example, the iterations are needed and convergence is not obtained otherwise. The benefit of the multi-scale procedure is clearly shown as well as the iterative scheme for each scale.

A nominal strain of 0.5 is now considered. This amplitude is too large for the procedure

---

[1] when a number $\Xi$ is written as $\Xi \pm \xi$, $\xi$ corresponds to the standard error

described above: it fails in one step with no additional treatment. Two different strategies are used to measure that strain:

- first, only the reference and deformed pictures are considered. However, the user is allowed to give a reference length $L_0$ and 'deformed' lengths $L_0 + \Delta L$ for the deformed pictures. This information is used to evaluate a first displacement field on scale no. $n = 4$. The average strain is equal to $0.503 \pm 0.001$ and the maximum error is equal to 2.1 gray levels (the average is equal to 0.6 gray level),
- second, an intermediate picture is added (its deformation corresponds to 0.25) and the reference picture is updated. This alternative is also successful (average strain: $0.502 \pm 0.001$) since strains of the order of 0.3 are measured without any problem with a good accuracy (the maximum error is here equal to 0.8 gray level and the average equals 0.2 gray level).

This simulation shows that, even though errors are cumulated when using more than one deformed image in an updating procedure, the second strategy is more robust than the first one. This is due to the fact that a 0.5 deformation is too high locally: the basic hypothesis of a constant local displacement is no longer valid. These two strategies will also be investigated in the following section devoted to the analysis of actual experiments.

## 5. Experiments on mineral wool samples

The above tests are quite satisfactory. However, by construction, there is no noise in the signal, and more importantly, the basic hypothesis (1) is met with $b(.) = 0$. However, in real cases, this assumption is only roughly satisfied, in particular when the images are obtained in a transmission mode. There is always a slight shift in contrast and in light intensity which may affect the overall efficiency. Furthermore, by construction, CCD cameras produce noise. Finally, the interpolated and prescribed displacements had the same shape. Therefore it is important to test the method by using realistic images for which strain heterogeneities occur. Compression experiments on stone and glass wool samples are analyzed below. Reflection and transmission illuminations are considered.

### A. Images in reflection

The first part deals with a series of pictures of three deformed stages of a $60 \times 200 \times 200$ mm$^3$ stone wool sample, the last deformed image is shown in Fig. 9 as well as the reference one. Since the product is crimped, the fibers are no longer oriented along a preferential direction. The density of the material studied herein is equal to 80 kg/m$^3$. The images are obtained in reflection. It follows that the corrections due to intensity variations are not needed in this first case. However, they are still used to check whether any bias is introduced. The pictures are taken by using a standard CCD camera ($336 \times 751$ pixels, 8-bit coding). Deformed picture no. 1 corresponds to an apparent strain of -0.083, which is evaluated by measuring the distance variation between upper and lower platens. Apparent strains of the order of -0.113 and -0.2 are obtained for pictures no. 2 and 3, respectively. It can be noted that the upper platen is not necessarily in contact with the sample for the reference picture, thereby inducing an uncertainty in the evaluation of the reference length $L_0$. Consequently, the chosen ROI does not include the two platens (Fig. 9). Even though these apparent strains are only orders of magnitude of the actual strain levels experienced by the stone wool sample, the maximum measurable strain for a gauge length of $7 \times 32 = 224$ pixels is of the order of 0.1

when $p = 5$. Consequently, a direct computation with no updating or additional information will fail *a priori*; *a posteriori* it did for the last picture (for which the actual average strain is of the order of $-0.13$). The two strategies introduced in Section 4. are also used in the present case.

Figure 10 shows the deformed mesh as well as contours of the error defined in Eq. (22) for the third deformed image. The first strategy leads to a maximum error equal to 10.7 gray levels (average: 1.2) that is greater than that given by the second (i.e., updating) strategy (average: 0.7 and maximum: 7.2 gray levels). The same tendency as that observed in Section 4 is found. The average strain level is equal to $-0.034 \pm 0.0008$ for the first picture (to compare with an apparent strain of $-0.083$). For the second image, the average is equal to $-0.056 \pm 0.001$ (to relate with an apparent strain of $-0.113$) and for the third image, $-0.128 \pm 0.005$ (to compare with an apparent strain of $-0.2$). These results show that a simple measurement based on apparent strains is not able to evaluate average strains in the sample. This difference is probably due to the evaluation of the reference gauge length $L_0$: the reference picture does not correspond to the point where the upper platen is in full contact with the sample (dark zones close to the platens in Fig. 9-a that disappear later, see Fig. 9-b). In practice, this moment is very difficult to determine. With the present results, it is possible to evaluate the gauge length by using the measured average strains and by keeping the measured separations of the platens for the deformed images. It follows that, for the two first images, a value of $283 \pm 1$ pixels is predicted. This reference length is drawn in Fig. 9-a and seems reasonable. For the third image, a value of 271 pixels is found. This presumably indicates that the test is no longer homogeneous as shown in Fig. 10. This hypothesis is confirmed by estimating the coefficient of variation (i.e., ratio of the standard deviation to the average strain) for the three stages: -0.025, -0.027 and -0.035, respectively.

In the present example, the multi-scale procedure allows for values of $p$ as small as 4. However, with this ZOI size, six analyzed points had a standard deviation of texture less than the prescribed limit. A conventional correlation technique would have required at least $p = 7$, thereby limiting the information concerning the strain heterogeneity in this kind of experiment. This corresponds to a second gain of the multi-scale approach when compared to classical DIC techniques. The results presented here are obtained in less than one minute for $3 \times 184$ ZOIs ($p = 5, \delta = 32$ pixels) on a Pentium II PC.

### B. Images in transmission

The second case used to test the method is a $140 \times 200 \times 50$ mm$^3$ sample of light glass wool (i.e., 6 kg/m$^3$ in the present case), which in its deformed state is uniaxially compressed. Images are obtained in transmission with no special preparation (Fig. 6). Moreover, due to the structure of the medium, the displacement field is essentially along the main contraction axis, and hence it is well-suited to the multi-scale analysis proposed in this study. Because of its low density, this material is used for its thermal insulation properties. For the same reason, it is severely compressed (i.e., more than 90%) and stored under high strains. The material must be able to recover most of its initial thickness after decompression to provide the required thermal insulation performances. The experimental procedure consists in applying a maximum displacement to the upper platen and to measure the residual strain when the displacement is removed. A sequence of 11 deformed states is considered.

At the end of the sequence, the apparent residual strain (i.e., $\Delta L/L_0$, see Fig. 6) is of the order of $-0.25$. This value should make it possible to perform a direct measurement between the reference and deformed images shown in Fig. 6. However, the texture variation during the experiment prevents this approach to be successful. Again, the two strategies of Section 4 are used. First, when the user is allowed to give a reference and deformed gauge length, the computation can be carried out in one step. However, a lot of points have their error greater than 4 gray levels, thereby limiting the analysis of the fluctuations of strains. An average strain of $0.2417 \pm 0.0002$ is obtained and a corresponding standard deviation of 0.0377. The average strain is consistent with a direct observation of the apparent strain. The average error is equal to 9.7 gray levels (maximum value: 71 gray levels). It follows that the displacements of numerous ZOIs are set to the interpolated value because the estimate is not accurate enough. Consequently, the estimate of the average strain is likely to be correct, but the fluctuations are not completely captured.

Since a sequence of 11 pictures is taken, an updating procedure can be followed. The ROI contains 840 ZOIs so that 9240 analyses on scale no. 1 are carried out (in less than two minutes when no iterations are used on each scale, and less than 5 minutes when iterations are allowed). An average strain of $-0.2501 \pm 0.0004$ is obtained and a corresponding standard deviation of 0.0470. The average error is equal to 2.5 gray levels (maximum value: 22 gray levels). This second set of results is more accurate than the first one. This is important when considering the fluctuations. Even though errors are cumulated when using the updating procedure, it is more robust because of texture variations. The change of the average strain and corresponding standard deviation for the whole sequence is shown in Fig. 11. When the maximum applied strain decreases, the average residual strain decreases and the corresponding standard deviation increases. Apart from the initial stages of compression, the standard deviation can be shown to increase in proportion to its mean value. More importantly, the volume elements which display a large (respectively small) residual strain as compared to the average, are the same in the sequence of images, thus revealing that weak (or strong) spots in the material remain weak (or strong) for all applied strains, and hence their mechanical performance is presumably due to a given microstructure.

When a sub-pixel procedure is used on scale no. 1, an average strain of $-0.2505 \pm 0.0004$ and a corresponding standard deviation of 0.0529 are measured. The average error is equal to 2.5 gray levels. The reference and deformed meshes are shown in Fig. 11. Figure 12 compares the deformed meshes for the final image of the sequence. First, the result obtained with an analysis of one image. The fluctuations are minimal as explained above (Figure 12-a). Second, Figure 12-b shows the results when no iterations are allowed in an updating procedure. The average strain is equal to $-0.2573 \pm 0.0004$ and the average error is equal to 2.5 gray levels. In this particular example, the iterations are not necessarily needed to get a reasonable estimate for the strain field. This is due to the fact that the strain variation between two pictures does not exceed 0.05. The effect of discarding the test on the error to keep a displacement estimate is shown in Fig. 12-c. The fluctuations increase since the standard deviation now equals 0.0601 for an average strain of $-0.2572 \pm 0.0004$ and an average error of 2.5 gray levels. In this case the fluctuations are higher, but still on the same order as a sub-pixel procedure. Finally, Fig. 12-d shows the effect of considering analyses for which the standard deviation of the ZOI can be very small. Few additional artifacts can be observed and lead to an increase of the standard deviation (i.e., 0.0607) for an average strain equal to $-0.2557 \pm 0.0004$ and an average error of 2.5 gray levels. Altogether, these four results are consistent with each other. Yet, if the strain fluctuations are sought, the two additional tests introduced in Section 3.D are very useful.

## 6. Conclusions

An improved procedure is introduced to determine displacement fields from the comparison of two images. It is based on a multi-scale approach of a homogeneous strain field in a tension or compression test. When a sub-pixel procedure is used, strains of the order of 0.0001 can be measured. The multi-scale approach enables the user to measure strain levels that are more important than with a conventional technique; the more the number of scales, the higher the maximum measurable strain. Furthermore, the texture variation is considered by checking the standard deviation of the zones of interest and introducing an error indicator, which is independent of the correlation procedure.

The method has been tested on two cases. A first artificial example where an actual texture has been deformed numerically, and a second based on real pictures of compressed glass wool samples. The first case gives accurate estimates of the displacement field when compared to a known displacement. Strain levels as high as 0.35 (or as low as -0.26) can be measured when only two images are considered and no strain fluctuations occur. For higher strain levels, the updating procedure is very robust, even though the errors are cumulated. In this example, it is also shown that the iteration procedure used on each scale is beneficial to the overall performance of the algorithm.

The second example shows a first situation dealing with stone wool samples for which the images are obtained in reflection. In this case, fluctuations occur and are measured with the multi-scale approach. In particular, it is shown that the higher the applied strain, the higher the corresponding standard deviation. The updating strategy turned out to be the most reliable because the region of interest was not too large (the number of scales involved did not allow for a direct measurement). The correlation technique yields a local information regarding the strains that can be compared to the local texture. The second situation, which is more complicated, corresponds to a glass wool sample compressed at different levels. Here, the images were obtained in transmission. Consequently, severe texture variations occur. Again, the updating procedure was the most robust strategy. It was possible to correlate the average permanent strain with the corresponding standard deviation.

Finally, it can be noted that the measurement of displacement and strain fields in experiments on mineral wool samples are only possible, up to now, thanks to digital image correlation. When large strains occur, which is usually the case, and/or texture variations, robust techniques are needed. Otherwise, the evaluation of the strain fluctuations cannot be estimated. The iterative multi-scale strategy was successful in the examples studied herein. It was also used to analyze multiaxial experiments on elastomers (e.g., PET) for which strains as high as 0.3 were measured between two images [32].

## Acknowledgments

The authors wish to acknowledge useful discussions with Prof. Y. Berthaud.

## References

1. L. Hesselink, “Digital image processing in flow visualization,” Ann. Rev. Fluid Mech. **20**, pp. 421-485 (1988).

2. R.J. Adrian, “Particle imaging techniques for experimental fluid mechanics,” Ann. Rev. Fluid Mech. **23**, pp. 261-304 (1991).

3. C.E. Willert and M. Gharib, “Digital particle image velocimetry,” Exps. in Fluids **10**, pp. 181-193 (1991).

4. N.A. Fomin, *Speckle Photography for Fluid Mechanical Measurements*, (Springer, Berlin (Germany), 1998).

5. M. Raffel, C.E. Willert and J. Kompenhans, *Particle Image Velocimetry, a practical guide*, (Springer, Berlin (Germany), 1998).

6. M.A. Sutton, W.J. Wolters, W.H. Peters, W.F. Ranson and S.R. McNeill, “Determination of displacements using an improved digital correlation method,” Im. Vis. Comp. **1**, pp. 133-139 (1983).

7. M.A. Sutton, S.R. McNeill, J.D. Helm and Y.J. Chao, “Advances in Two-Dimensional and Three-Dimensional Computer Vision,” in *Photomechanics*, P.K. Rastogi, ed., (Springer, Berlin (Germany), 2000), pp. 323-372.

8. P.T. Tokumaru and P.E. Dimotakis, “Image correlation velocimetry,” Exps. in Fluids **19**, pp. 1-

15 (1995).

9. S. Roux, F. Hild and Y. Berthaud, “Correlation image velocimetry: A spectral approach,” Appl. Opt. **41**, pp. 108-115 (2002).

10. T.C. Chu, W.F. Ranson, M.A. Sutton and W.H. Petters, “Applications of digital-image-correlation techniques to experimental mechanics,” Exp. Mech. **3**, pp. 232-244 (1985).

11. D.J. Chen, F.P. Chiang, Y.S. Tan and H.S. Don, “Digital speckle-displacement measurement using a complex spectrum method,” Appl. Opt. **32**, pp. 1839-1849 (1993).

12. Y. Berthaud, J. Scholz and J. Thesing, “Méthodes optiques et acoustiques de mesures des caractéristiques mécaniques,” in*Proc. Colloque national MECAMAT Mécanismes et mécanique des grandes déformations*, (1996), pp. 77-80.

13. F.P. Chiang, Q. Wang and F. Lehman, “New developments in full-field strain measurements using speckles,” in *Non-Traditional Methods of Sensing Stress, Strain and Damage in Materials and Structures* (ASTM, Philadelphia (USA), 1997), **STP 1318**, pp. 156-169.

14. D. Choi, J.L. Thorpe and R. Hanna, “Image analysis to measure strain in wood and paper,” Wood Sci. Technol. **25**, pp. 251-262 (1991).

15. C. G’Sell, J.-M. Hiver, A. Dahnoun and A. Souahi, “Video-controlled tensile testing of polymers and metals beyond the necking point,” J. Mat. Sci. **27**, pp. 5031-5039 (1992).

16. L. Chevalier, S. Calloch, F. Hild and Y. Marco, “Digital image correlation used to analyze the multiaxial behavior of rubber-like materials,” Eur. J. Mech. A/Solids **20**, pp. 169-187 (2001).

17. G. Holst, *CCD Arrays, Cameras and Displays*, (SPIE Engineering Press, Washington DC (USA) 1998).

18. B. Wagne, S. Roux and F. Hild, “Spectral approach to displacement evaluation from image analysis,” Eur. Phys. J. AP **17**, pp. 247-252 (2002).

19. B.K.P. Horn and B.G. Schunck, “Determining optical flow,” Artificial Intelligence **17**, pp. 185-203 (1981).

20. A. Mitiche and P. Bouthemy, “Computation and analysis of image motion: A synopsis of current problems and methods,” Int. J. Comp. Vision. **19**, pp. 29-55 (1996).

21. P.J. Hubert, *Robust Statistics*, (Wiley, New York (USA) 1981).

22. M. Black, *Robust Incremental Optical Flow*, Ph.D. dissertation, Yale University, 1992.

23. J.-M. Odobez and P. Bouthemy, “Robust multiresolution estimation of parametric motion models,” J. Visual Comm. Image Repres. **6**, pp. 348-365 (1995).

24. D. Bogen and D. Rahdert, “A strain energy approach to regularization in displacement field fits of elastically deforming bodies,” IEEE Trans. Pattern Analysis and Machine Intelligence **18**, pp. 629-635 (1996).

25. L.C. Gui and W. Merzkirch "A comparative study of the MQD method and several correlation-based PIV evaluation algorithms," Exps. in Fluids **28**, pp. 36-44 (2000)

26. R. Hill, "Aspects of invariance in solid mechanics," Adv. Appl. Mech. **18**, pp. 1-75 (1978).

27. R.D. Keane and R.J. Adrian, "Optimization of particle image velocimeters. Part I: Double pulsed systems," Meas. Sci. Technol. **1**, pp. 1202-1215 (1990).

28. Matlab, *Matlab 5.3, the Language of Technical Computing, version 5.3*, (the MathWorks, inc., http://www.mathworks.com, 1999).

29. J.-N. Périé, S. Calloch, C. Cluzel and F. Hild, "Analysis of a multiaxial test on a C/C composite by using digital image correlation and a damage model," to appear in Exp. Mech. (2002).

30. J. Bolinder, *On the accuracy of digital particle image velocimetry system*, technical report, Lund Institute of Technology, **ISSN 0282 - 1990** (1999).

31. D.P. Hart, "Super-resolution PIV by recursive local correlation," J. Visual. **10**, pp. 1-10 (1990).

32. Y. Marco, L. Chevalier and M. Chaouche, "X-Ray stuy of induced cristallisation and orientation in PET under biaxial loading: Application to blow-moulding process," in *Proc. 5th International ESAFORM Conference on Material Forming*, M. Pietryk, Z. Mitura and J. Kaczmar, eds., (Akapit, Krakow (Poland), 2002), pp. 227-230.

## List of Tables

1 Average nominal strain $\overline{E}_{yy}$ and corresponding standard deviation $\overline{\overline{E}}_{yy}$ for different sizes of ZOIs ($\delta = 16$ pixels) predicted by a conventional DIC technique. A pixel procedure is used. The prescribed strain $E_{yy}$ is equal to 0.05. . . . . 32

Table 1. Average nominal strain $\overline{E}_{yy}$ and corresponding standard deviation $\overline{\overline{E}}_{yy}$ for different sizes of ZOIs ($\delta = 16$ pixels) predicted by a conventional DIC technique. A pixel procedure is used. The prescribed strain $E_{yy}$ is equal to 0.05.

| | $\overline{E}_{yy}$ | $\overline{\overline{E}}_{yy}$ |
|---|---|---|
| p = 4 | 0.0014 | 0.003 |
| p = 5 | 0.0419 | 0.0006 |
| p = 6 | 0.0456 | 0.0004 |
| p = 7 | 0.0470 | 0.0001 |

## List of Figures

1 (a) Initial and (b) artificially deformed ($E_{yy} = 0.05$) images of a stone wool sample. The Region Of Interest ($ROI_{\text{ref}}$) and two Zones Of Interest ($ZOI_{\text{ref}}$ and $ZOI_{\text{def}}$) are depicted. Four centers of ZOIs are shown on the reference picture ($\delta$: separation between neighboring ZOIs). . . . . . . . . . . . . . . . . 35

2 Flowchart of the principal steps in a conventional correlation algorithm. . . 36

3 Standard deviation of the vertical displacement vs. vertical position $y$ of the ZOI when a strain $E_{yy} = 0.05$ is prescribed (Fig. 1). A classical digital image correlation procedure is used for different sizes ($2^p \times 2^p$ pixels) of the zones of interest ($\delta = 16$ pixels). . . . . . . . . . . . . . . . . . . . . . . . . . . . 37

4 Different notations used in the multi-scale approach. Sub-ROI of a reference image (scale no. 2) and corresponding super-images on scales nos. 3, 4. . . . 38

5 Flowchart of the principal steps in the multi-scale correlation algorithm. . . 39

6 Initial (a) and last ‘deformed’ (b) images of a glass wool sample. The reference length $L_0$ and the length variation $\Delta L$ are drawn. . . . . . . . . . . . . . . . 40

7 Vertical displacement (○) and corresponding standard deviation (●) vs. vertical position $y$ of the ZOI when a strain $E_{yy} = 0.35$ is prescribed. The multi-scale correlation procedure is used ($p = 4, \delta = 16$ pixels). . . . . . . . . . . . . . 41

8 Average strain vs. iteration number for different sizes $(2^p \times 2^p)$ pixels of the zones of interest and shifts $\delta$. The dashed line corresponds to a simulation in which no iteration is used for a given scale. The arrows show the first time a scale, the level of which is indicated by the numbers close to the arrows, is invoked. A strain $E_{yy} = 0.35$ is applied. . . . . . . . . . . . . . . . . . . . . . . . 42

9 Reference and deformed images of a stone wool sample. The estimated reference length $L_0$ is drawn. . . . . . . . . . . . . . . . . . . . . . . . . . . . . . 43

10 Reference and deformed meshes of a stone wool sample predicted by using two strategies of the multi-scale approach and corresponding error contours: (a) no image update, (b) with two image updates. The black square depicts one ZOI ($p = 5, \delta = 32$ pixels). . . . . . . . . . . . . . . . . . . . . . . . . . 44

11 (a) Average residual strain vs. standard deviation of a compressed glass wool sample. (b) Reference and deformed meshes at the end of the sequence ($p = 5, \delta = 32$ pixels). . . . . . . . . . . . . . . . . . . . . . . . . . . . . . . . . 45

12 Comparison of reference and deformed meshes at the end of the sequence of a compressed glass wool sample ($p = 5, \delta = 32$ pixels). Four different options are used in the multi-scale approach: (a) no image update, (b) with image update and no iteration, (c) with image update and no limitation on $\eta$ and (d) with image update and no test on the local texture fluctuations. . . . . . 46

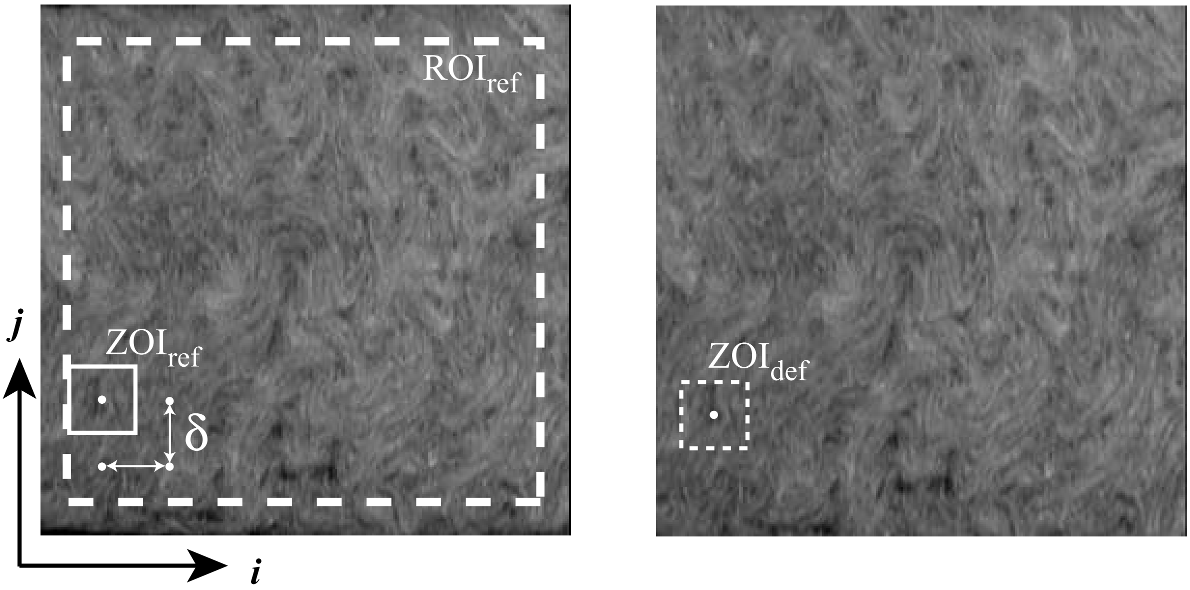

-a-

-b-

Fig. 1. (a) Initial and (b) artificially deformed ($E_{yy} = 0.05$) images of a stone wool sample. The Region Of Interest ($ROI_{\mathrm{ref}}$) and two Zones Of Interest ($ZOI_{\mathrm{ref}}$ and $ZOI_{\mathrm{def}}$) are depicted. Four centers of ZOIs are shown on the reference picture ($\delta$: separation between neighboring ZOIs).

Hild et al.

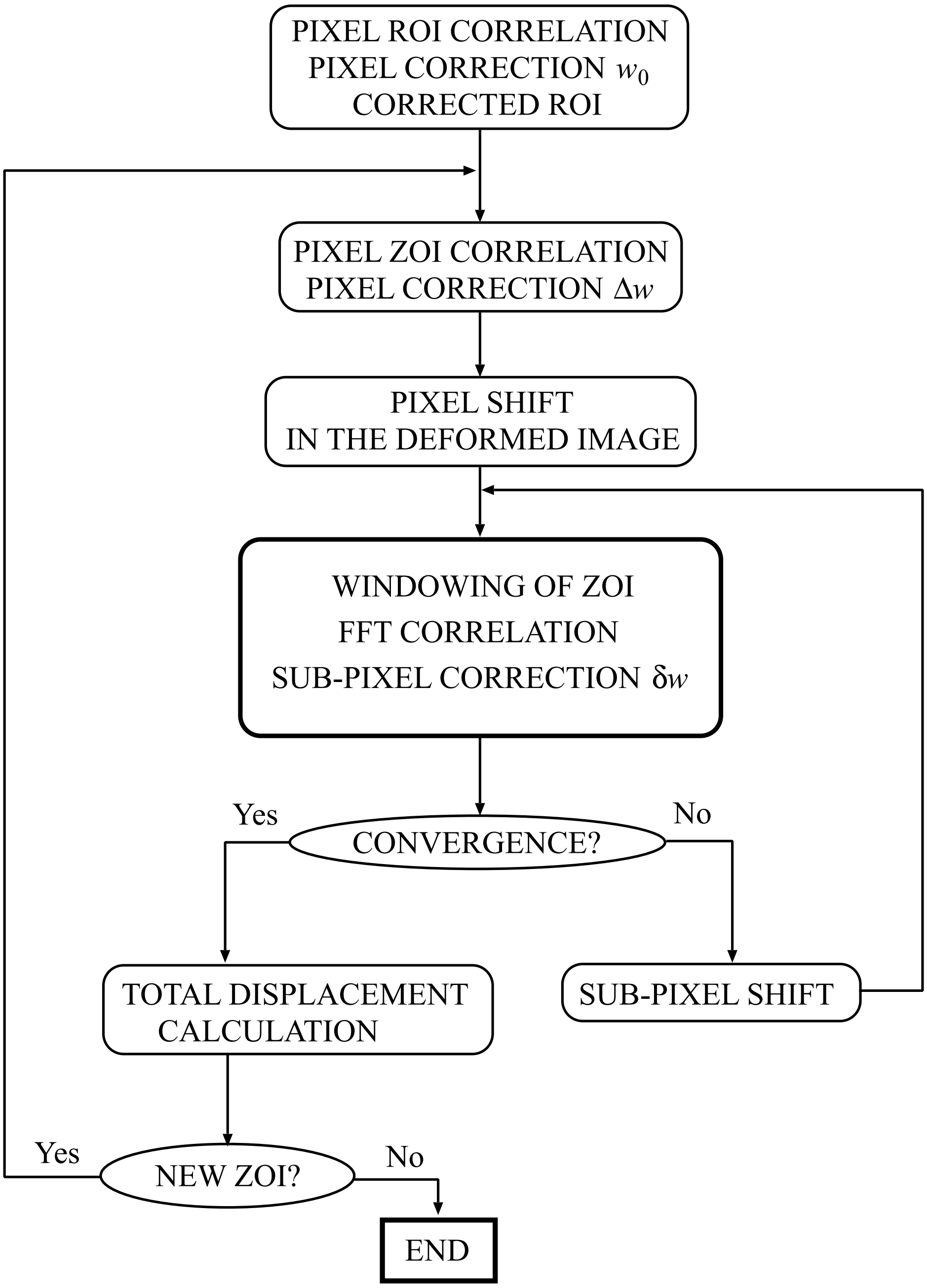

Fig. 2. Flowchart of the principal steps in a conventional correlation algorithm.

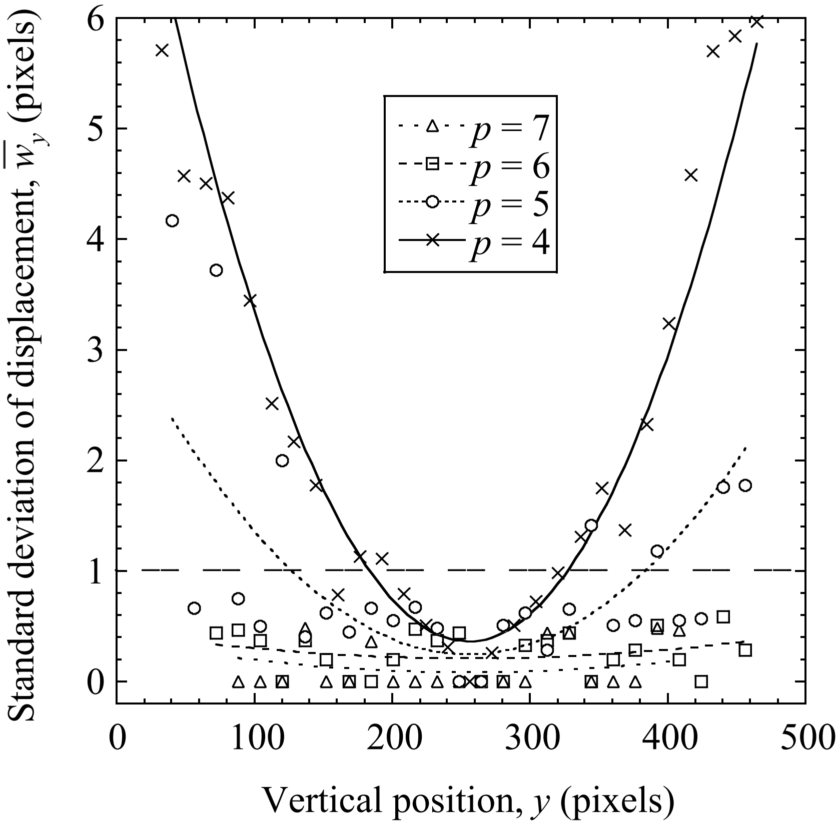

Fig. 3. Standard deviation of the vertical displacement vs. vertical position $y$ of the ZOI when a strain $E_{yy} = 0.05$ is prescribed (Fig. 1). A classical digital image correlation procedure is used for different sizes ($2^p \times 2^p$ pixels) of the zones of interest ($\delta = 16$ pixels).

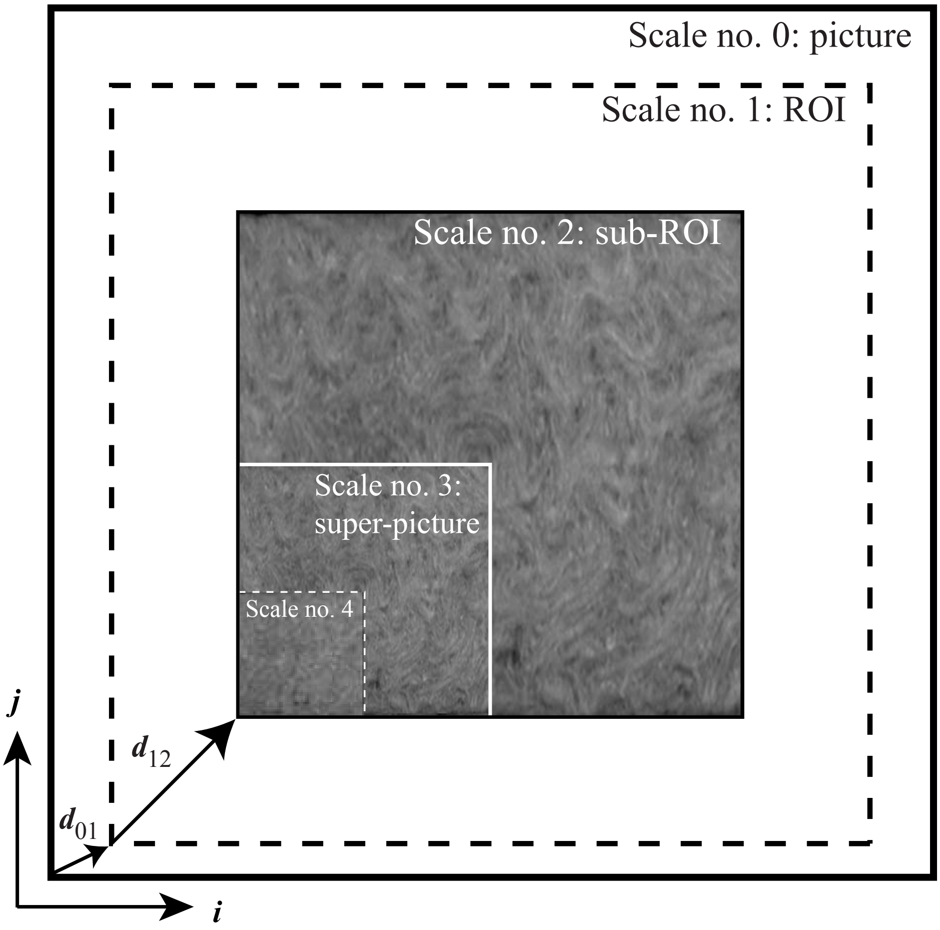

Fig. 4. Different notations used in the multi-scale approach. Sub-ROI of a reference image (scale no. 2) and corresponding super-images on scales nos. 3, 4.

Hild et al.

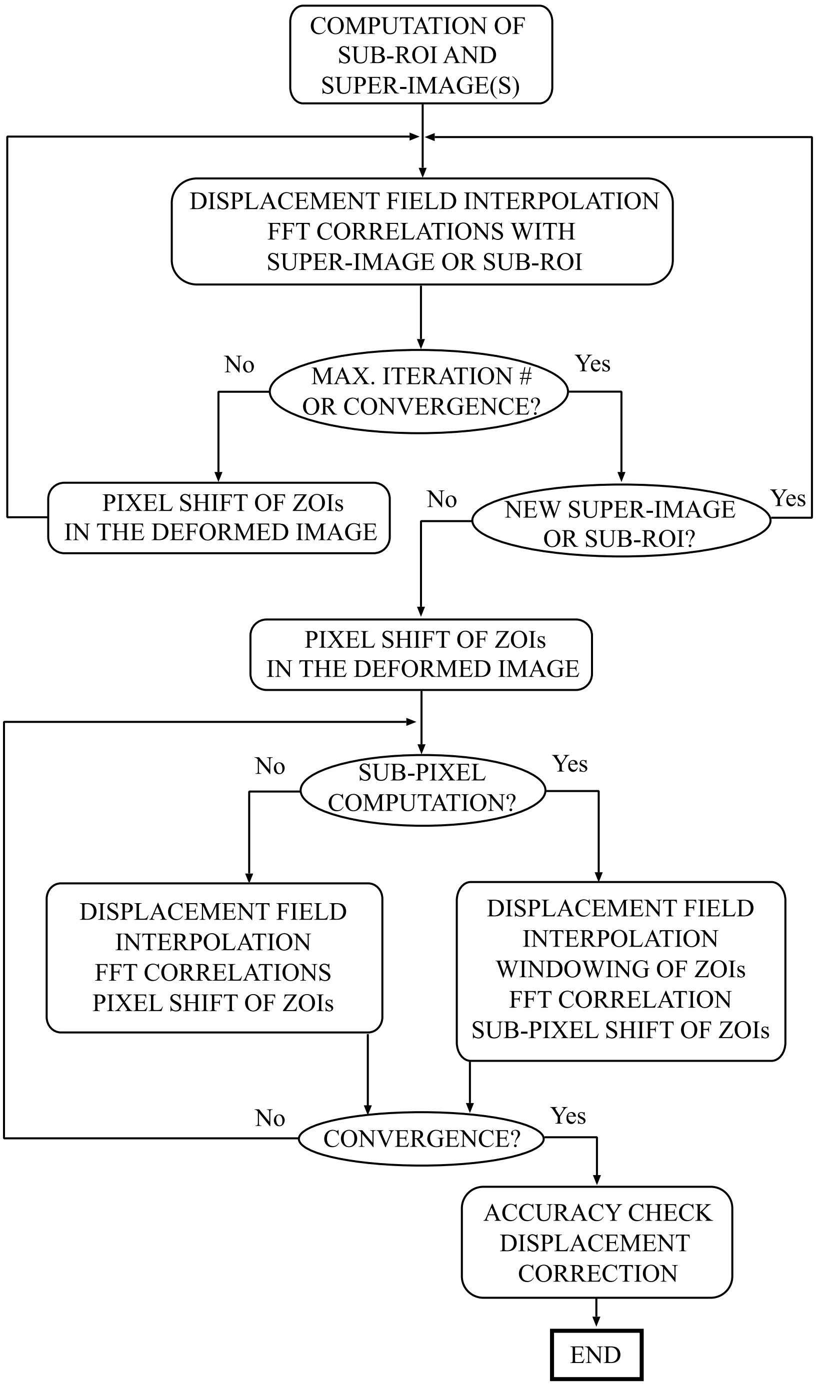

Fig. 5. Flowchart of the principal steps in the multi-scale correlation algorithm.

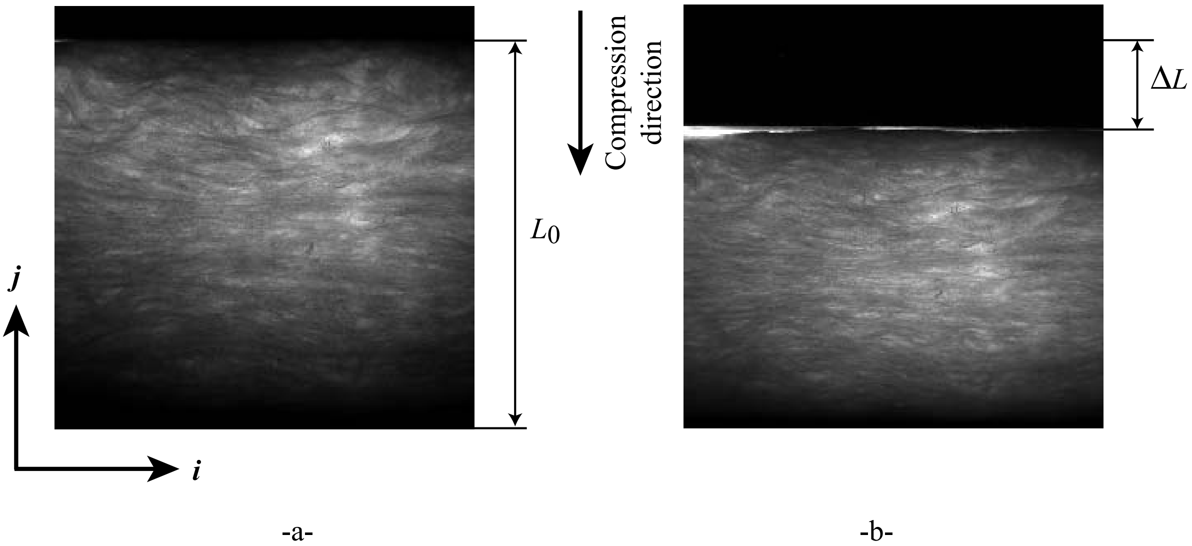

-a- -b-

Fig. 6. Initial (a) and last 'deformed' (b) images of a glass wool sample. The reference length $L_0$ and the length variation $\Delta L$ are drawn.

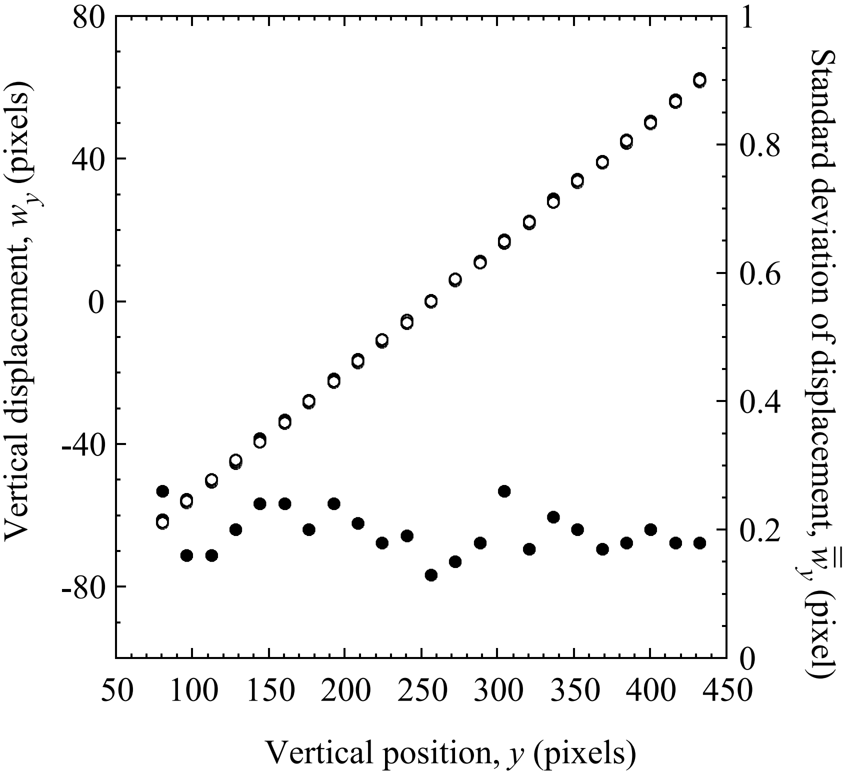

Fig. 7. Vertical displacement (○) and corresponding standard deviation (●) vs. vertical position $y$ of the ZOI when a strain $E_{yy} = 0.35$ is prescribed. The multi-scale correlation procedure is used ($p = 4, \delta = 16$ pixels).

Hild et al.

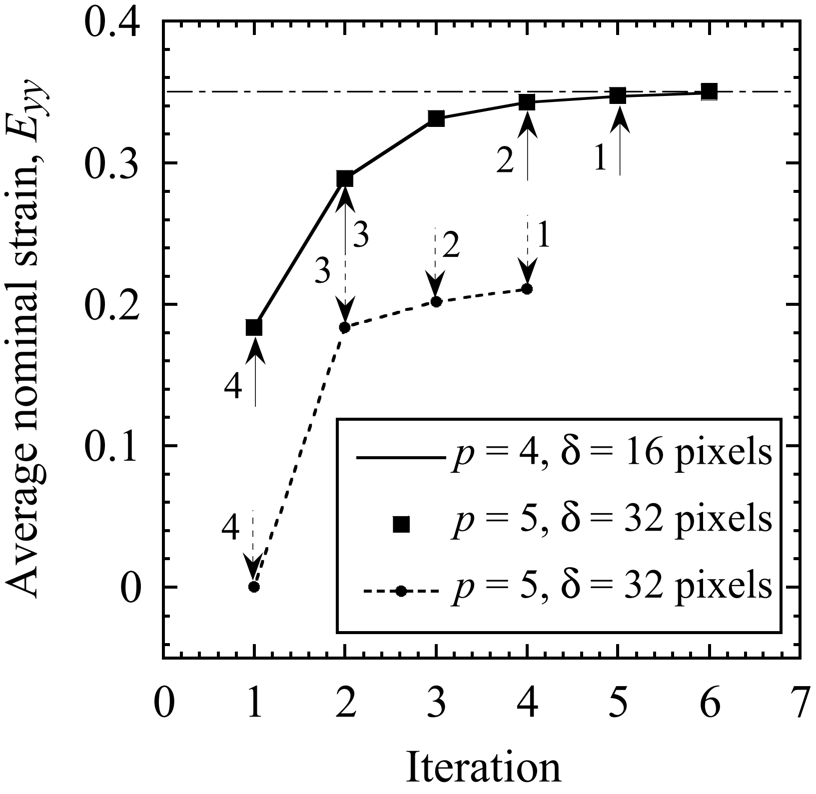

Fig. 8. Average strain vs. iteration number for different sizes ($2^p \times 2^p$) pixels of the zones of interest and shifts $\delta$. The dashed line corresponds to a simulation in which no iteration is used for a given scale. The arrows show the first time a scale, the level of which is indicated by the numbers close to the arrows, is invoked. A strain $E_{yy} = 0.35$ is applied.

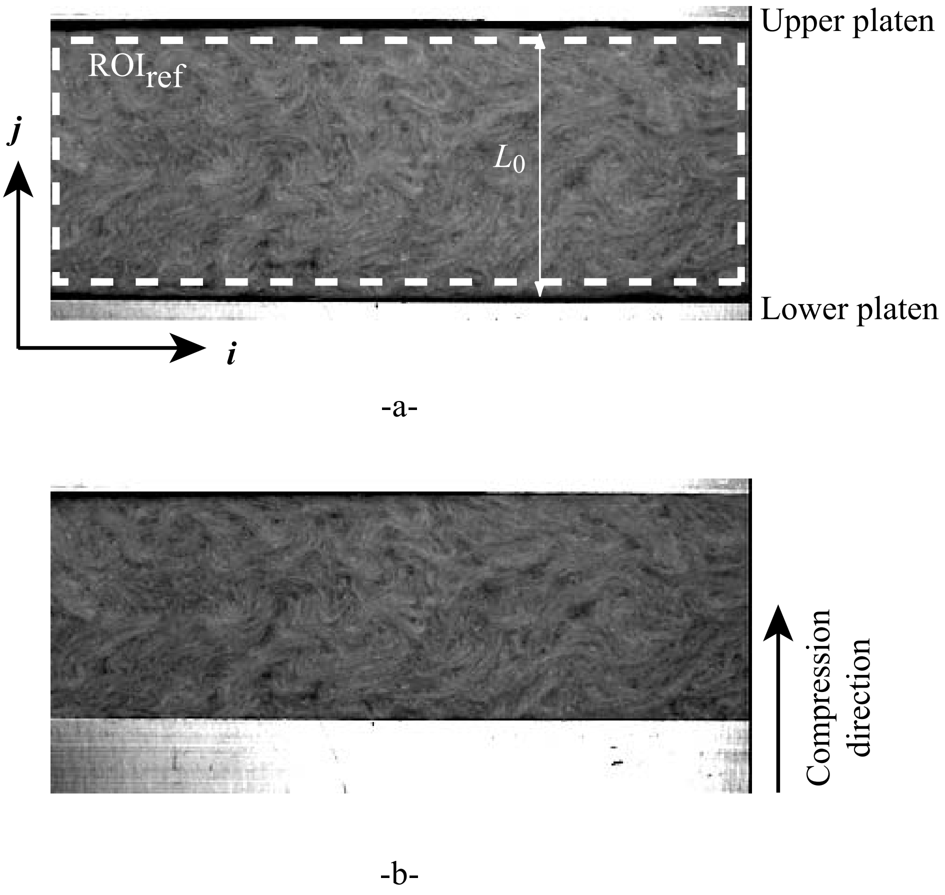

Fig. 9. Reference and deformed images of a stone wool sample. The estimated reference length $L_0$ is drawn.

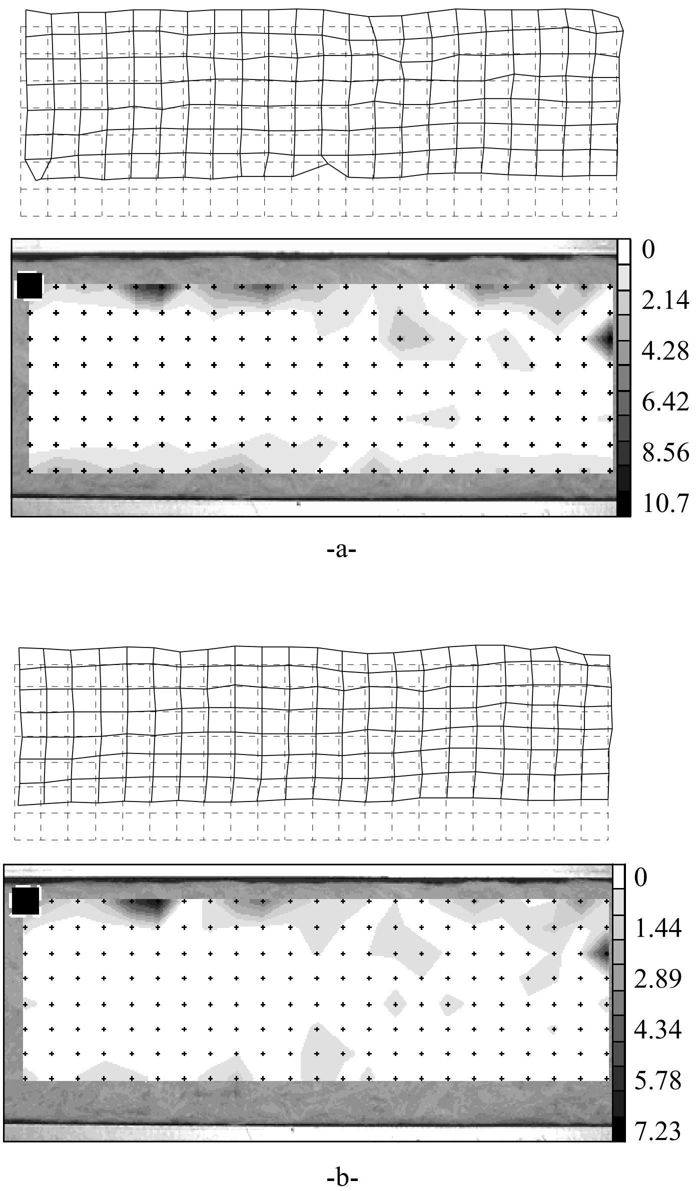

Fig. 10. Reference and deformed meshes of a stone wool sample predicted by using two strategies of the multi-scale approach and corresponding error contours: (a) no image update, (b) with two image updates. The black square depicts one ZOI ($p = 5, \delta = 32$ pixels).

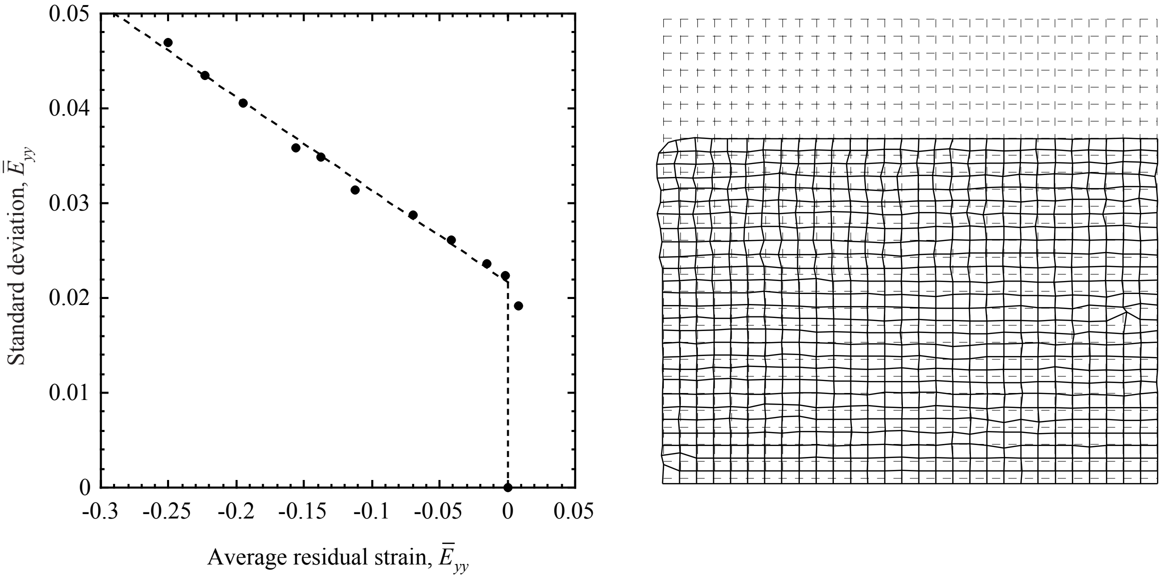

-a-

-b-

Fig. 11. (a) Average residual strain vs. standard deviation of a compressed glass wool sample. (b) Reference and deformed meshes at the end of the sequence ($p = 5, \delta = 32$ pixels).

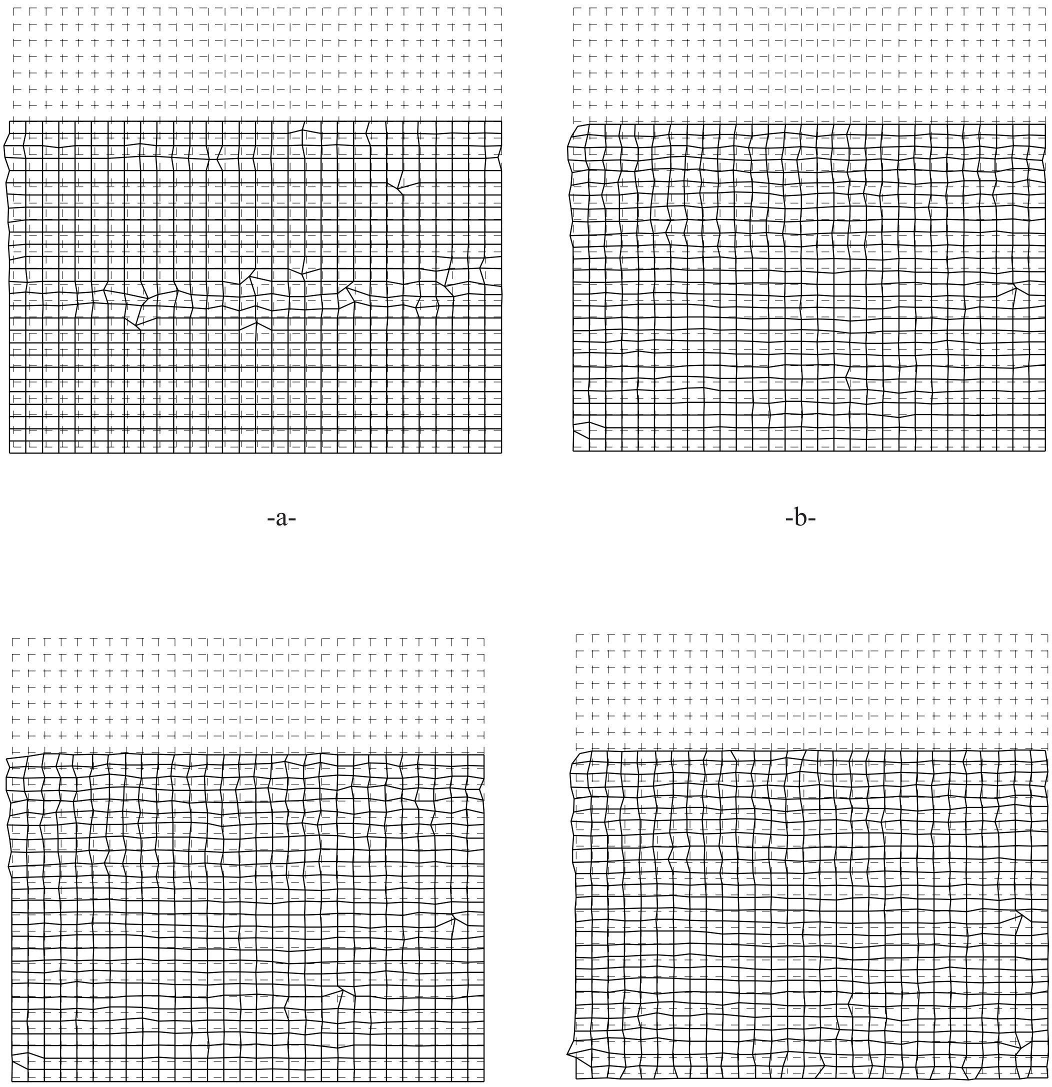

-a- -b-

-c- -d-

Fig. 12. Comparison of reference and deformed meshes at the end of the sequence of a compressed glass wool sample ($p = 5, \delta = 32$ pixels). Four different options are used in the multi-scale approach: (a) no image update, (b) with image update and no iteration, (c) with image update and no limitation on $\eta$ and (d) with image update and no test on the local texture fluctuations.